Modeling of Casting, Welding and Advanced Solidification Processes - XI
Edited by Charles-André Gandin and Michel Bellet
TMS (The Minerals, Metals & Materials Society), 2006

SIMULATION OF INCLUSION AND BUBBLE MOTION IN A STEEL CONTINUOUS CASTER

Claudia Pfeiler[1], Menghuai Wu[1], Andreas Ludwig[1], Christian Chimani [2], Josef Watzinger [2], Helmut Dösinger [3]

[1]Christian-Doppler Laboratory for Multiphase Modelling of Metallurgical Processes, Department of Metallurgy, University of Leoben; Franz-Josef-Str. 18; 8700 Leoben, Austria
[2]VOEST-Alpine Industrieanlagenbau GmbH & Co, Turmstr. 44; 4031 Linz, Austria
[3]RHI Refractories, Magnesitstr. 2; 8700 Leoben, Austria

Keywords: bubble, continuous casting, discrete phase, inclusion, solidification, mold

Abstract

During steel continuous casting non-metallic inclusions and argon gas, which is intentionally injected into the submerged entry nozzle (SEN) to avoid the attraction of liquid air and nozzle clogging, are brought into the mold. If they become trapped in the solidified strand they can cause undesired defects in the final casting product. This paper presents a numerical approach to couple the 3D turbulent flow, the transport of the inclusions/bubbles and the solidification of the strand. A 3D turbulent Euler-Lagrangian model is used to calculate the trajectories of continuously injected inclusions and gas bubbles in the submerged entry nozzle and the mold area of a steel continuous caster. An enthalpy-porosity method is used to simulate the solidification. The model considers momentum and energy exchanges between the melt and the inclusions/bubbles. Interaction of inclusions/bubbles with the mushy zone and entrapment of the inclusions/bubbles into the solidified shell are numerically described. Simulation results of a continuous caster at engineer scale near the SEN region are presented and discussed.

Introduction

Non-metallic inclusions are originated from deoxidation, reoxidation and exogenous processes in previous melt treatment processes, while argon gas bubbles are intentionally injected into the nozzle to avoid attraction of ambient air [1]. The main concern is the transport of inclusions and gas bubbles in the melt pool. If the flow pattern is carefully adjusted by an optimized submerged entry nozzle (SEN) and/or optimized casting parameters, the melt flow may carry the inclusions and bubbles to the liquid slag layer, where they might be removed. Otherwise, they will eventually be trapped by the solidification front and cause undesired defects in the final product. Great modeling efforts were made to study the melt flow in the molten pool [1, 2-4] and, very recently, also to investigate directly the influence of the flow on the transport of inclusions [5-10]. Most of these publications consider only the impact of the melt flow on the trajectories of the inclusions, while the influence of the inclusions on the flow is ignored. Former studies of the authors have shown that bidirectional influences affects the melt flow pattern significant [11].
Several investigations have been reported also on the interaction between such inclusions and a solid/liquid interface during solidification [12-19]. It is pertinent for optimizing process control and product quality to understand the interactions between the evolving solid phase and the inclusions/bubbles in the melt. In-Situ measurements in experiments using CCD camera [12], digital microscope [13] or laser microscope for metals [14] have determined the critical interface velocity for pushing or engulfment and the movement of inclusions/bubbles from or into the solidified front. Considering turbulent flow the engulfment of inclusions shows probabilistically

behavior [15]. Numerical small scale investigations have been done to estimate the inclusions and solid/liquid interaction [16-19]. For industrial purpose it is important to have an engineering scale simulation which can predict the amount, size, type and entrapment regions of inclusions. Only recently the entrapment under engineering scale is modeled. The solidification fronts are simplified as flat wall boundaries [6, 20]. Yuan and Thomas [20] have considered three additional forces acting on inclusions near the wall. However, it is known that the behavior of an inclusion/bubble depends also significantly on the shape of the solid/liquid interface [21, 22]. Therefore, the purpose of the present study is to describe the behavior of inclusions and bubbles during the calculated transient solidification process in engineering scale and with that to estimate the concentration of inclusions/bubbles in the solidified shell.

Model Description

Flow Dynamics

Mass and momentum conservation equations for an incompressible fluid are given by

$$\nabla \cdot \vec{u} = 0 \tag{1}$$

$$\frac{\partial(\rho\vec{u})}{\partial t} + \vec{u}\nabla(\rho\vec{u}) = -\nabla p + \mu_{eff}\nabla^2\vec{u} + \vec{F} + S \tag{2}$$

where $\mu_{eff} = \mu + \mu_t$ is the effective viscosity due to turbulence, for which the standard k-ε model is used. μ is the dynamic viscosity and ρ density of the melt, $\vec{u}$ is the velocity, p is the static pressure and $\vec{F}$ is a momentum source term which accounts for the presence of inclusions and/or bubbles as expressed in Eq. (6). S is the momentum sink due to solidification (Eq. 12). The turbulent viscosity, μ_t, is defined by $\mu_t = \rho C_\mu k^2/\varepsilon$ with $C_\mu = 0.09$. In the standard k-ε turbulence model the time-averaged velocity field is solved together with equations for the transport of turbulent kinetic energy, k, and its dissipation, ε [23].

Transport of Inclusions/Bubbles

Inclusions and bubbles are considered as discrete secondary phases with spherical geometry disperse distributed in the melt. The trajectories of these discrete phases are computed by integrating the equation of motion in a Lagrangian frame

$$\frac{d\vec{u}_p}{dt} = \frac{18\mu}{\rho_p d_p^2}\frac{C_D \,\mathrm{Re}}{24}\left[(\vec{u} + \vec{u}') - \vec{u}_p\right] + \frac{\vec{g}\cdot(\rho_p - \rho)}{\rho_p} \ . \tag{3}$$

Here, $\vec{u}_p$ is the velocity, d_p the diameter and ρ_p the density of the considered discrete phase. $\vec{g}$ is the gravity and $\vec{u}'$ is the fluctuating velocity component defined in Eq. (7). The trajectory of an individual discrete object is based on the forces acting as it moves through the flow. The terms on the right-hand side of Eq. (3) represent drag force and buoyancy force. For the drag coefficient, C_D, the following approach is taken [24]

$$C_D = a_1 + \frac{a_2}{\mathrm{Re}} + \frac{a_3}{\mathrm{Re}^2} \ . \tag{4}$$

Here, a_1, a_2 and a_3 are constants that apply to smooth spherical inclusions/bubbles over several ranges of Re. The relative Reynolds number, Re, is defined as

$$\mathrm{Re} = \frac{\rho d_p \left| \vec{u}_p - \vec{u} \right|}{\mu} \ . \tag{5}$$

The momentum transfer from the discrete phases to the melt is computed by examining their momentum change as

$$\vec{F} = \sum_i^N \frac{18 \mu C_D \mathrm{Re}}{\rho_p d_p^2 24} (\vec{u}_p - \vec{u}) \dot{m}_p \Delta t \ . \tag{6}$$

Here, N is the number of inclusions and/or bubbles in a computational cell and $\dot{m}_p$ is the mass flow rate of inclusions and/or gas bubbles.
The dispersion of the inclusions and/or bubbles due to turbulence in the melt is treated using a stochastic tracking model. This stochastic tracking model includes the impact of instantaneous turbulent velocity fluctuations, $u'(t)$, on the trajectories. The fluctuating velocity components are discrete piecewise constant functions of time. Their random value is kept constant over an interval of time given by the rotation time of an eddy. This rotation time, τ_e, which describes the time an inclusion/bubble spent in the turbulent motion of the considered eddy, is proportional to the discrete phase dispersion rate. For the k-ε model the rotation time can be expressed according to [25] as $\tau_e \approx 0.3 \cdot k / \varepsilon$. The values of the fluctuations in 3-dimension u', v' and w' that prevail during the lifetime of the turbulent eddy are sampled by assuming that they obey a Gaussian probability distribution, so that

$$u' = \varsigma \sqrt{\frac{2k}{3}} \qquad v' = \varsigma \sqrt{\frac{2k}{3}} \qquad w' = \varsigma \sqrt{\frac{2k}{3}} \tag{7}$$

where ζ is a normally distributed random number. The discrete phase crossing time is defined as

$$t_{cross} = -\tau \cdot \ln \left[1 - \left(\frac{L_e}{\tau \cdot \left| u - u_p \right|} \right) \right] \tag{8}$$

where τ is the discrete phase relaxation time and L_e is the eddy length scale. The inclusion/bubble is assumed to interact with the melt eddy over the smaller of the eddy rotation time and the eddy crossing time. When this time limit is reached, a new value of the instantaneous velocity is obtained by applying a new value of ζ in Eq. (7).

Solidification Model

Instead of tracking the liquid-solid front explicitly, an enthalpy-porosity formulation is used to model solidification. This formulation is provided by the commercial Software Fluent [26]. The mushy zone is treated as a porous zone with porosity equal to the liquid fraction f_l calculated using the lever rule.

$$f_l = \frac{T - T_S}{T_L - T_S} . \tag{9}$$

The latent heat L depends on the liquid fraction in a computational cell. The enthalpy H of the material is then defined as

$$H = h_{ref} + \int_{T_{ref}}^{T} c_p dT + f_l L \tag{10}$$

Where c_p is the specific heat, h_{ref} is the reference enthalpy at the reference temperature T_{ref}. The energy conservation equation considering solidification is written as

$$\frac{\partial}{\partial t}(\rho H) + \nabla(\vec{u}\rho H) = \nabla(k_{eff}\nabla T). \tag{11}$$

Here, k_{eff} is the effective conductivity which is defined as $k_{eff} = k + k_t$, where k is the thermal conductivity of the material and k_t is the turbulent thermal conductivity. Momentum sink terms are added to the momentum equation to account for the pressure drop caused by the presence of solid material. The momentum sink in the mushy zone takes the following form:

$$S = \frac{(1-f_l)^2}{f_l^3} A_{mush}(\vec{u} - \vec{u}_{pull}) \tag{12}$$

Here, A_{mush} is the mushy zone constant measuring the amplitude of damping. $\vec{u}_{pull}$ is the constant casting velocity of the solidified strand. Sinks are also added to all of the turbulence equations in the mushy and solidified areas with the term $(\vec{u} - \vec{u}_{pull})$ being replaced by correspond terms for k or ε. Due to the resulting high drag coefficient between the melt and the non-metallic inclusions/bubbles (Eq. 4) corresponding to the melt viscosity, which is a linear function of temperature from liquidus to solidus, inclusions/bubbles are forced to follow the melt flow in the mushy zone. When the rest melt is transformed to solid, the inclusions/bubbles follow the pull velocity u_{pull} of the solidified strand. This velocity of them is equal to the casting speed. The entrapment of the inclusions/bubbles is modeled in this way.

Computation Details

The full three dimensional calculation domain consists of a trifurcated submerged entry nozzle (SEN), a mold pool zone of 1 m in length and a following secondary cooling zone of 1.5 m in length.

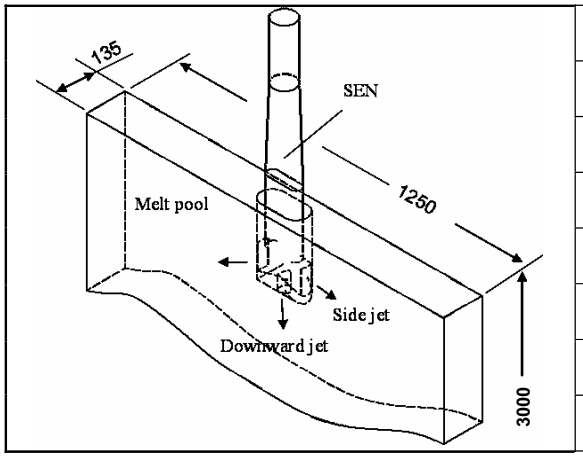

slab width	1250	mm	casting temperature	1837	K
slab thickness	135	mm	latent heat	243	kJ/kg
slab length	2500	mm	inclusion density	3700	kg/m³
SEN length	832	mm	inclusion diameter	10, 500	µm
SEN submerged depth	160	mm	inclusion mass flow	1.2E-03	kg/s
casting speed	2.5	m/min	bubble density	0.19	kg/m³
solidus temperature	1789	K	bubble diameter	4000	µm
liquidus temperature	1807	K	gas volume flow	4	l/min

Figure1. Considered geometrical and process parameters.

Temperature dependent properties of the steel melt such as material viscosity, density, specific heat and thermal conductivity are taken from the IDS software (commercial solidification analysis package, Helsinki University) assuming that the steel composition corresponds to low carbon steel. The computation domain has been discretized with a structured and an unstructured mesh which consists of 600.000 cells. The inlet is positioned at the top surface of the trifurcated SEN. From there all inclusions and bubbles are injected. Two different size classes of alumina inclusions and one size class of argon gas bubbles are introduced. The geometrical and process parameters are shown in Figure 1. At the inlet a flat velocity profile and at the bottom of the calculation domain a constant pressure boundary condition is applied. The top surface of the liquid melt pool being in contact with the casting slag is supposed to be flat. Here, a free-slip condition is used. Inclusions and bubbles are modeled as to be caught at the top surface and at the SEN walls. These walls are assumed to be insulating. At the mold walls a heat flux function and for the secondary cooling zone a constant heat-transfer coefficient refer to industrial values are used. The solidified shell is modeled to move downwards with a constant casting speed. At the outlet the solid strand is pulled out of the domain.

Results And Discussions

Figure 2 shows the velocity field at the wide central plane. Transient simulation was carried out with time step Δt = 0.005 s, and 20 iteration per time step. Although a 3D and slightly unsymmetrical grid is used, the transient procedure converged to steady and symmetrical solution is obtained. The liquid melt emerges from the inlet of the nozzle, divides through the trifurcated SEN into two side and one center jets. The two side jets are divided at the narrow mold, and build as usual the upper and the lower roll in continuous casting molds.

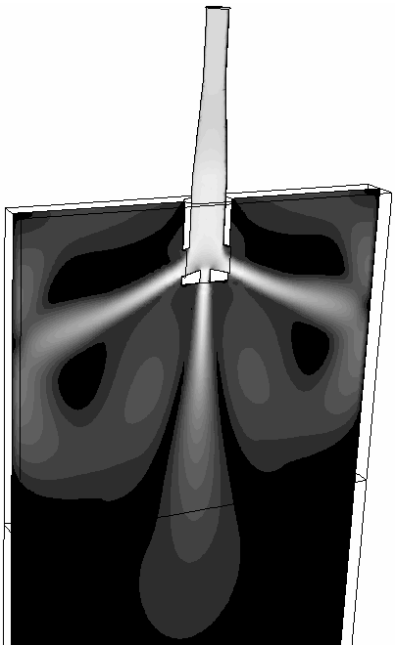

Figure 2. Contours of velocity magnitude in gray scale: black for minimum (0) and white for maximum (2.25 m/s).

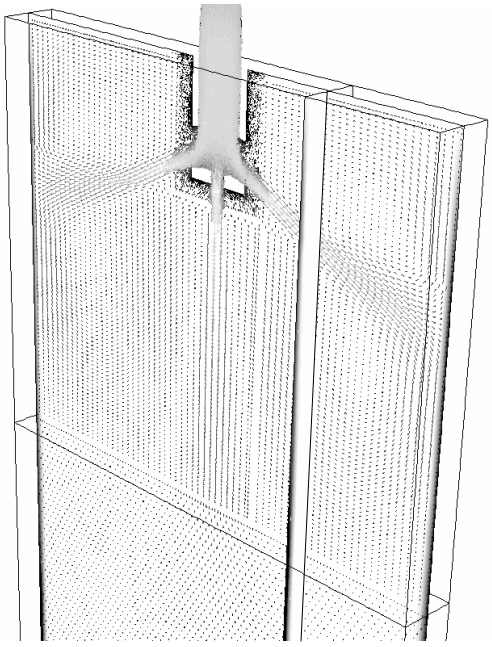

Figure 3. The solid fraction f_s in two vertical sections is shown in gray scale: white for 0 and black for 1. The velocity vectors on the wide central plane are also shown.

The steady state solidification sequence is shown in Figure 3. The solid fraction f_s distribution on the wide central plane and a vertical thickness section shows that the solid shell (f_s = 0.8) starts to build about 0.08 m from the meniscus and becomes thicker with the slab length.

Alumina inclusions and argon bubbles start to be injected from the top inlet f the SEN after a steady state solidification and fluid flow have been achieved. The distribution of alumina inclusions and gas bubbles in the whole 3D domain of the slab is shown in Figure 4 after 14 seconds of injection time. Two different size classes of alumina inclusions (10 μm, 500 μm) and one size of bubbles (4000 μm) were injected. A large difference of the flow behavior is observed between inclusions and bubbles. Due to the large buoyancy force acting on bubbles, they moved upwards directly out of the nozzle and are captured by the slag surface. A significant amount of bubbles seem to be captured at the top of the nozzle side ports. Comparing the two different size classes of the alumina inclusions, we find that the larger inclusions can also move more easily move upwards to the slag surface. There are more large inclusions which are collectively distributed in the region of near the slag surface than the small inclusions. The position of the large inclusions which are brought downwards by the center jet is higher than the position of the small inclusions.

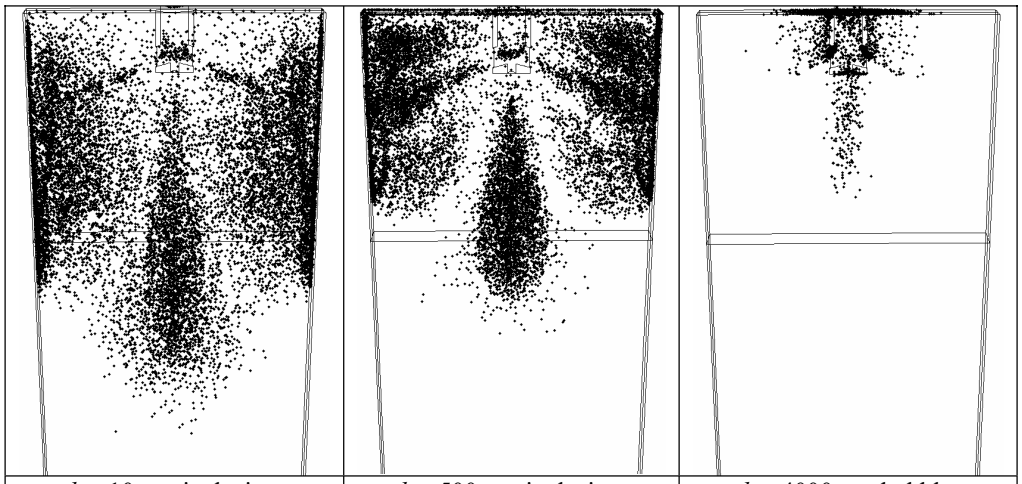

d_p = 10 μm inclusions	d_p = 500 μm inclusions	d_p = 4000 μm bubbles
n = 17.000 inclusions	n = 17.000 inclusions	n = 17.000 bubbles

Figure 4. Inclusion and bubble distribution in the slab after t = 14 seconds of injection time. The inclusions and the bubbles are injected from the top inlet of the SEN.

In order to demonstrate the potential of the recent model for the prediction of the inclusions which are entrapped in the solidified strand, a transient result of the inclusion mass concentration after t = 14 seconds of injection time is shown (Figure 5). The mass flow rate of the small alumina inclusions (10 μm) is constituted to $\dot{m}$ = 5.9 x 10^{-4} kg/s at the top inlet of the SEN. To distinguish the inclusions which are entrapped in the solidified strand from those which are still in the melt, the line of zero strength s (f_s = 0.8*)* is also shown in Figure 5. The particles below the line are entrapped in the strand, while those above are still in the mushy zone or in the melt. The simulation result shows that the mass concentration entrapped in the solidified strand is strongly influenced by the melt flow. High inclusion entrapment rates are located in the areas where the three jets of the trifurcated nozzles point to. Because the considered inclusions are quite small, i.e. 10 μm, the relative velocity between the inclusions and the melt caused by the buoyancy force is small, so that the inclusions following the main jets are quickly brought to the solidification fronts and are frozen in the solidified strand before they are able to float up. The inclusions which are branched into the side streams (not following the main streams of the jets) are relatively calm, and have longer time to move up. As seen in the thickness sections a and b of Figure 5, it seems that there are more inclusions in solidified strand than in the melt. The explanations are as follows. The solid shell starts to form just above the jets. Because the mass concentration of inclusions in the regions where the shell forms is relatively high, many

inclusions are entrapped. These inclusions move in the solidified strand downwards and are brought to lower regions.

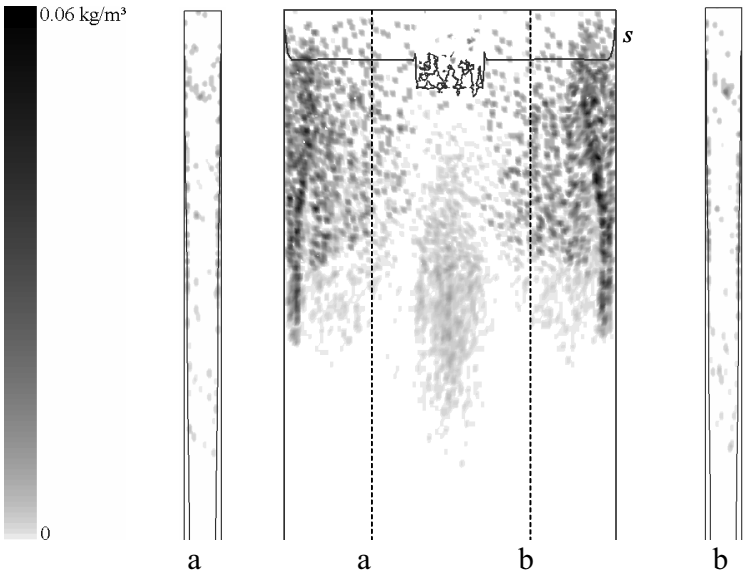

Figure 5. Distribution of mass concentration of inclusions at three different sections: one at a wide slab surface; two vertical thickness sections (a, b) which are located 0.3 m left and right from the nozzle center. The length of the slab shown here is 2 m. Here only the transient mass concentration of the small inclusions (d_p = 10 μm) at t = 14 s after the first injection is shown. The lines of zero strength s (f_s = 0.8) at the surfaces are also plotted.

The above preliminary results have confirmed the potentials of the numerical model. It combines the turbulent melt flow, transport of the inclusions/bubbles, the transient solidification process, and the entrapment of the inclusions and bubbles in the solidifying strand. However, in order to apply this model to industry, systematical parameter studies are necessary such as grid sensitivity, etc. The numerical models for the drag law between the inclusions/bubbles and the melt, for the mechanical interaction between inclusions/bubbles and the mushy zone, and for the solidification by a simple linear $f_s - T$ function need to be improved in future.

In the present model the effect of the discrete phase on the flow is taken into account, but the influence on turbulence is ignored. The validity of the stochastic tacking model depends on the inclusion size versus the turbulence scales. Eddies that are larger than the inclusion size are usually damped, while smaller are enforced. For inclusions smaller than the Kolmogorov scale (smallest eddy), the viscosity dissipation is strong enough so that there is no influence on the turbulence. In our case, the range of turbulence scale is between 1250 mm and $2\text{x}10^{-4}$ mm (Kolmogorov scale). The inclusion sizes considered are 10^2~10^3 times bigger than the Kolmogorov scale, but 10^4~10^5 times smaller than the largest scale of the turbulence. This means that there are enough eddies enhancing the mixing rate, so that a stochastic model can be used to model the mixing. The gas bubbles are in a different situation, they are 10^4 bigger than the Kolmogorov scale, but 10^3 times smaller than the biggest eddies. The use of the stochastic tracking model for the bubbles is possible but less rigorous than for the inclusions.

Conclusions

An Eulerian-Lagrangian model for the transport of the non-metallic inclusions and inert gas bubbles in a continuous caster and the entrapment of these inclusions/bubbles into the solidified shell has been presented. Benchmark simulations of steel continuous casting at engineer scale near the SEN region are carried out, and following conclusions are made.

1. The enthalpy-porosity solidification model in the Eulerian frame can be coupled with DPM (dispersed particle model) model in the Lagrangian frame to predict the entrapment of inclusions/bubbles into the solid strand of a continuous caster.
2. The transport of inclusions/bubbles depends strongly on the size and the density of them. Larger and lighter inclusions/bubbles are easier to float upwards, and more likely captured by the slag at the slag-melt interface. The smaller inclusions are coupled more strongly with the flow, and are more dispersedly distributed in the caster, hence they are more likely entrapped into the solidifying strand.
3. The melt flow shows to have a strong influence on the entrapment of inclusions in the strand. The areas of the high inclusion entrapment rate are mainly located in regions around the center jet and the side jets.

Acknowledgements

This work is financially supported by the Austrian Christian-Doppler (CD) Research Society for which the authors kindly acknowledge. The authors are grateful to Dr. Braun and Dr. Postl with FLUENT Deutschland GmbH, Darmstadt, Germany, for their excellent technical assistance. Finally, thanks are due to Dr. Kharicha of University of Leoben for his support and knowledge in modeling.

References

1. B.G. Thomas. *Modeling for Casting and Solidification Processing,* ed. K.O. Yu (New York, NY: Marcel Dekker, Inc., 2002), 499-539.
2. A. Ramos-Banderas et al., *Metall. Mat. Trans*., 35B (2004), 449-460.
3. Q. Yuan et al., *Steel Res. Int*., 76 (2005), 33-43.
4. Q. Yuan, B.G. Thomas, and S.P. Vanka, *Metall. Mat. Trans*., 35B (2004), 685-702.
5. Q. Yuan, B.G. Thomas, and S.P. Vanka, Metall. *Mat. Trans*., 35B (2004), 703-714.
6. M. Javurek et al., *Steel Res. Int*., 76 (2005), 64-70.
7. D. Mazumdar and R.I.L. Guthrie, *Metall. Mat. Trans*., 25B (1994), 308-312.
8. A. Mukhopadhyay et al., *Steel Res. Int*., 76 (2005), 22-32.
9. M.P. Schwarz, *Appl. Math. Modelling*, 20 (1996), 41-51.
10. A. Alexiadis, P. Gardin, and J. F. Domgin, *Metall. Mat. Trans*., 35B (2004), 949-956.
11. C. Pfeiler, M. Wu, and A. Ludwig, *Mater. Sci. Eng. A*, 413-414 (2005) 115-120.
12. S. Kimura et al., *Metall. Mat. Trans*., 31B (2000), 1013-1021.
13. H. Esaka et al., *ISIJ Int.*, 44 (4) (2004), 682-690.
14. Y. Wang and S. Sridhar, *Ironmaking and Steelmaking*, 30 (3) (2003), 223-228.
15. H. Yasuda, I. Ohnaka, and H. Jozuka, *ISIJ Int.*, 44 (8) (2004), 1366-1375.
16. M. Ode et al., *ISIJ Int.*, 40 (2) (2002), 153-160.
17. L. Hadji, *Metall. Mat. Trans*., 35A (2004), 2181-2185.
18. S. Mukherjee and D.M. Stefanescu, *Metall. Mat. Trans*., 35A (2004), 613-621.
19. S. Mukherjee and D.M. Stefanescu, *Metall. Mat. Trans*., 35A (2004), 623-629.
20. B.G. Thomas et al., *Proceedings of 2004 NFS DMII Grantees Conference*, (Scottsdale, Arizona, 2004).
21. A.W. Rempel and M.G. Worster, *J. Cryst. Growth*, 223 (2001), 420-432.
22. J.W. Garvin and H.S. Udaykumar, *J. Cryst. Growth*, 252 (2003), 451-466.
23. B.E. Launder and D.B. Spalding, *Computer Methods in Applied Mechanics and Engineering*, 3 (1974), 269-289.
24. S.A. Morsi and A.J. Alexander, *J. Fluid Mech*., 55 (2) (1972), 193-208.
25. B.J. Daly and F.H. Harlow. *Phys. Fluids*, 13 (1970), 2634-2649.
26. Fluent Inc. *FLUENT 6.2 Users's Guide*, http://www.fluent.com, Lebanon, USA (2005).